mathematics

MDPI

Article

The Squeeze Film Effect with a High-Pressure Boundary in Aerostatic Bearings

Yangong Wu, Jiadai Xue, Zheng Qiao, Wentao Chen and Bo Wang *

Center for Precision Engineering, Harbin Institute of Technology, Harbin 150001, China
* Correspondence: bradywang@hit.edu.cn

Abstract: The squeeze film effect was discussed in several fields, but mostly under the same pressure boundary conditions. However, pressures at the inlet and outlet are different for aerostatic bearings. In this paper, the dynamic Reynolds equation group, with the stiffness and damping pressure written separately, is deducted and numerically solved with a high-pressure boundary for a parallel flat and circular thin film. The circular thin film considers the two results of the supply pressure boundary inside and outside. All dynamic pressure distribution and stiffness curves are given in a dimensionless form, and a comparative analysis of squeeze film characteristics with and without external pressure is conducted. From the calculation results, it can be concluded that the squeeze effect shows damping for zero-frequency and stiffness for infinite-frequency for compressible lubricants. The dynamic pressure in the static high pressure region is also high at high frequencies affected by gas compressibility. Based on these analytical results, the transfer functions of the thin film are given to further analyze the dynamic performance of aerostatic bearings, and the shape of the response curve approximates an exponential decay form, even when the amplitude increases to 10% of the gas film thickness.

Keywords: squeeze films; Reynolds equation; numerical analysis; dynamic performance; aerostatic bearings

MSC: 35M12

Citation: Wu, Y.; Xue, J.; Qiao, Z.; Chen, W.; Wang, B. The Squeeze Film Effect with a High-Pressure Boundary in Aerostatic Bearings. *Mathematics* **2023**, *11*, 742. https://doi.org/10.3390/math11030742

Academic Editor: Panayiotis Vafeas

Received: 20 December 2022
Revised: 29 January 2023
Accepted: 31 January 2023
Published: 1 February 2023

1. Introduction

When two surfaces separated only by a thin air film have relative normal motion, the air film has a reaction force against surfaces to block movement tendency, which is the squeeze film effect. The squeeze film effect is reflected in many mechanical parts, with the common feature being that all of the boundary is at atmospheric pressure.

For example, the squeeze film damping effect is quite important at ball raceway contact in ball bearing; the damping of ball bearings is mainly derived from the squeeze film effect [1–3]. The squeezed film at ball raceway contact is an inherent characteristic of ball bearings and may also occur at the contact of the outer ring with a bearing seat. When the outer ring of the bearing is designed to slide freely and bear an additional load of the axial thermal expansion, there is a small gap in the outer ring of the bearing, and the squeeze film effect is more obvious. The air damping effect of micro-electromechanical systems (MEMSs) is also very obvious. Micro-electromechanical systems such as micro-accelerometers and micro-gyroscopes are limited by technology and packaging conditions, and their moving structures generally work in an environment with a certain gas pressure. As the characteristic size of a micro-structure shrinks, its surface area-to-volume ratio gradually increases, and the air damping effect becomes extremely significant [4]. In the capacitive micro-machined accelerometer described in [5], when the central plate moves up and down, the air caught in the gap between the plates is squeezed, then force is exerted on both plates, and the squeeze film effect can be significant, which provides effective

damping in a wide-frequency band. Besides these two cases, a squeeze film before clutch contact affects its performance. A wet clutch soaks the disc in the transmission oil, adopts oil-immersed heat dissipation, and has a high heat dissipation efficiency. However, the oil medium delays the physical contact between the parallel disc clutch surfaces, and its performance is seriously affected [6,7]. The squeeze film effect also contributes to tire slipping on wet roads. When a car drives over a water-covered road, the lubricating effect of the water film significantly reduces the coefficient of the friction between a tire and road, and the tires are then prone to slipping. When the tire speed exceeds a certain limit value, the dynamic pressure generated by the water flow is sufficient to lift the tire off the ground. Once hydroplaning occurs, tires will completely lose their drive and braking forces [8]. Similarly, walking with rubber soles on wet or icy surfaces leads to similar problems [9]. Typical examples of making full use of the squeeze film effect are squeeze film dampers and vibro-tactile texture reproduction techniques. A squeeze film damper is installed between the rolling bearing and support structure, and an oil gap is formed between the outer rings of connected oil film. Squeeze oil film dampers can effectively absorb the vibration energy of rotors and ensure their smooth operation. It is one of the most important research achievements affecting high-speed rotor dynamics in recent decades. At present, squeeze film damping technology is widely used in high-speed rotating machinery such as aero-engines, turbo-compressors, and industrial gas engines [10]. Texture tactile reproduction is a specific hardware device that generates physical stimuli that act on users when in contact with a textured surface, thereby simulating the surface characteristics of objects such as roughness, hardness, and viscosity. Texture haptic technology is used to generate ultrasonic waves via a touch screen, and the squeeze film effect is used to create an air gap between the user's finger and the display, thus reducing the friction and increasing smoothness [11]. It can be seen that the principle of this technique is identical to that of squeeze film bearings.

There is one common feature in the aforementioned occasions where the squeeze film effect exists: all of the boundary is at atmospheric pressure, or more precisely, the boundary pressure is the same. The problem with constant pressure boundary conditions has previously been studied [12,13], in particular by Langlois [14], Gross [15], Pan [16], and Blech [17]. However, for externally pressurized air bearings (EPABs), the pressure decreases from a high-pressure in the inlet to an atmosphere condition in the outlet, which possesses different characteristics compared with the same-pressure boundary. In the early days of air bearing development, discussions of stability were mainly aimed at understanding whether a bearing is affected by a pneumatic hammer or at assessing the stability margin [18,19]. There has been much interest in evaluating the damping capacity of bearings, which is quite critical because EPABs are famous for having relatively little damping. Analytical, numerical, and experimental methods were used to study the dynamic performance of EPABs. In addition to experiments, in general, there are two methods used to solve the dynamic characteristics of an EPAB: one is the time-linearization or perturbation method, and the other is the time-domain iterative method. The system is solved through the time domain response and the dynamic stiffness parameters are identified from it. The basic idea of the perturbation method is to superimpose a gap change caused by displacement or velocity in the steady-state gap as a small disturbance, and to approximate the transient Reynolds equation with a small amount, ignoring all high-order terms [20]. The dynamic characterization of EPABs includes an evaluation of stiffness and damping coefficients as a function of excitation frequency. A change in bearing capacity obtained by dynamic pressure integration divided by the disturbance value is the dynamic stiffness of the gas film. Licht first used the perturbation method to test the accuracy of lumped parameter models of single-bore thrust bearings [21]. Boffey analyzed the effect of additional rubber rings using Licht's calculation method, noting that external damping can improve stability [22], which was experimentally verified [23]. The advent of high-performance calculation technology made it possible to build complex numerical models. Stiffler modeled the feedhole boundary between the central disk region

and the exterior annular region as a line source, and the dynamic pressure distribution of rectangular and circular EPABs were investigated [24,25]. Miyatake and Yoshimoto used computational fluid dynamics (CFD) technology to numerically simulate the static and dynamic performance of a circular EPAB with small feed holes [26]. By introducing the concept of an infinitesimal radius, Bhat overcame the mathematical difficulty of the conformal transformation of disc thrust gas bearing center point by the finite element method (FEM), analyzed the dynamic characteristics of the capillary-restricted air bearing pad, and determined the dynamic stiffness with the disturbance frequency [27]. These distributed parameter models can be used to accurately analyze and solve for the dynamic characteristics of EPABs, but cannot provide a direct link between design parameters and the performance index. The influence of different parameters on the dynamic characteristics of bearings is coupled together, and it is difficult to form a systematic design method. To solve this problem, Colombo et al. proposed a simple lumped parameter (LP) model of infinite parallel plates [28], which is based on the discretization of the Reynolds equation and treats the parallel plates as a combination of gas tank and pneumatic restrictors. This simple LP model is able to correctly predict the damping capacity, unlike the analytical solution. This basic idea has been adopted to predict the dynamic performance of EPABs, which can be seen as an assembly of orifices and gas film [29–31]. Starting from this point, if we can determine the influence of various parameters of the bearing on its transfer function, then the dynamic performance of EPABs can be appropriately designed, according to the zero-pole configuration of the control system.

It should be noted that the boundary conditions for normal orifice-type aerostatic bearings dynamically change, since an orifice not only generates high pressure but also controls the mass flowing into the gas film surface, which is a major difference from the constant pressure boundary found in this paper. In fact, the dynamic characteristics of the gas film solved in this paper are a simplification of a special kind of orifice-type bearing known as surface-restriction aerostatic bearings, whose main feature is that the boundary pressure is different, but the external pressure is constant. There are very few studies on this type of gas bearing, and there is no research on its dynamic characteristics. In this paper, the squeeze film effect of thin films inside EPABs with a high-pressure boundary is determined, and compared with that of same-boundary conditions. For both boundary types, this paper offers an important view on the dynamic performance of air bearings: air bearings behave according to the squeeze number. For low squeeze numbers, when the exciting frequency is low or the film is thick, the viscous forces dominate, and the air is sucked in or forced out of the film when the air gap height oscillates. If there is no orifice, the air gap should be treated as a viscous damper. For high squeeze numbers with an increase in exciting frequency or with small air gaps, the compressibility effects become stronger, which makes the air gap behave like a spring. The key to analyzing the squeeze film problem is to determine the time-dependent pressure distribution inside the film caused by the relative motion. When gas compressibility is considered, the results of the squeezed film solution are complicated, and its properties cannot be intuitively seen, even for a simple disk boundary. Therefore, this paper aimed to calculate the dynamic pressure distribution for common components of EAPBs, i.e., infinite long thin films and circular films considering both inside flow and outside flow.

2. The Compressible Reynolds Equation and Its Perturbation Form

2.1. Reynolds Equation

When the bearing speed is small or the bearing is not moving, the aerodynamic effect can be neglected, and the Reynolds equation considering the ideal gas compressibility can be expressed as [32]:

$$\nabla \cdot \left(\frac{h^3}{12\eta} P_{\text{abs}} \nabla P_{\text{abs}} \right) = \frac{\partial (h P_{\text{abs}})}{\partial t} \tag{1}$$

Here, ∇ is the Laplacian operator, h is the thin film thickness, η is the dynamic viscosity of the lubricants, and P_{abs} is the absolute pressure inside a thin film.

The expansion of Equation (1) in the Cartesian coordinate system is [32]:

$$\frac{\partial}{\partial x}\left(\frac{h^3}{12\eta}P_{\text{abs}}\frac{\partial P_{\text{abs}}}{\partial x}\right)+\frac{\partial}{\partial y}\left(\frac{h^3}{12\eta}P_{\text{abs}}\frac{\partial P_{\text{abs}}}{\partial y}\right)=\frac{\partial(hP_{\text{abs}})}{\partial t} \tag{2}$$

The expansion of Equation (1) in the cylindrical coordinate system is [32]:

$$\frac{1}{r}\frac{\partial}{\partial r}\left(\frac{h^3}{12\eta}rP_{\text{abs}}\frac{\partial P_{\text{abs}}}{\partial r}\right)+\frac{1}{r}\frac{\partial}{\partial \theta}\left(\frac{h^3}{12\eta}\frac{1}{r}P_{\text{abs}}\frac{\partial P_{\text{abs}}}{\partial \theta}\right)=\frac{\partial(hP_{\text{abs}})}{\partial t} \tag{3}$$

When solving the static characteristics of EPABs, the term on the right side of Equation (1) is zero. Using the differential equation $f\mathrm{d}f=\mathrm{d}f^2/2$, it can be expressed with the pressure square P_{abs}^2 as the variable [33]:

$$\frac{\partial}{\partial x}\left(h^3\frac{\partial P_{\text{abs}}^2}{\partial x}\right)+\frac{\partial}{\partial y}\left(h^3\frac{\partial P_{\text{abs}}^2}{\partial y}\right)=0 \tag{4}$$

2.2. The Perturbation Form of the Reynolds Equation

The general problem of fluid lubricated bearings can be analyzed in terms of the three following aspects [34]: (a) steady-state conditions; (b) transient operating conditions; and (c) effects due to small-amplitude harmonic changes in geometry. The steady-state conditions are the starting point of all calculations, describing the conditions for a balanced operation of the entire system. This step requires the calculation of the bearing capacity, friction loss, mass flow rate, etc. The transient operating conditions are considered for the time-transient solution of a coupled dynamical system, and the results can be used to obtain dynamic stability or study the nonlinear behavior in the case of large offsets.

The position of an air bearing is not fixed. In the process of cutting or under micro-shocking, the bearing vibrates regularly around the equilibrium position. According to Newton's second law, the dynamic displacement of the air film can be calculated by the following formula:

$$h_1=v_0t+\int\frac{W_1(h_1(t))+\text{external force}}{M}\mathrm{d}t^2,\quad W_1=\iint P_{\text{abs1}}\mathrm{d}\Omega \tag{5}$$

The direct calculation of the above formula not only includes a the space integral of dynamic pressure distribution, but also includes the time integral of the position change, which relatively complicates the solution process. The effects due to small-amplitude harmonic changes in the geometry are considered to determine the motion of the bearing in the normal direction of the air film and only determines the dynamic behavior linearized near a given operating point; that is, the response process of the bearing after a small impact is analyzed, and the perturbation method is used to handle the time term in the Reynolds equation [20]. Note that variables such as the pressure and clearance in the gas film are linearly superimposed by the steady-state item and the time-varying perturbation item, that is:

$$P_{\text{abs}}=P_{\text{abs0}}+P_{\text{abs1}},\quad h=h_0+h_1 \tag{6}$$

The subscript 0 indicates the steady-state item, which is completely unrelated to time t. The subscript 1 indicates the dynamic item, and the amplitude of the dynamic item is much smaller than the steady-state item. The perturbation method linearizes the dynamic behavior of the air film near the steady-state operating point, and the superposition of the input leads to the superposition of the output. Therefore, various tools in the linear system can be used to analyze the characteristics of the system. The gas film is equivalent to the superposition of a spring and damper, and the stiffness and damping characteristics of the gas film are solved first.

By bringing the expression of the variable in Equation (6) into Equation (2) and omitting the high-order small amount, the steady-state Reynolds Equation (4) and perturbation equations can be obtained, respectively [35]:

$$2\,\nabla\cdot\left[h_0^3\nabla(P_{\mathrm{abs0}}P_{\mathrm{abs1}})\right]+3\,\nabla\cdot\left[h_0^2h_1\nabla\left(P_{\mathrm{abs0}}^2\right)\right]=24\eta\left(h_0\frac{\partial P_{\mathrm{abs1}}}{\partial t}+P_{\mathrm{abs0}}\frac{\partial h_1}{\partial t}\right) \quad (7)$$

We can transpose and rearrange the equations as follows:

$$-h_0\frac{\partial P_{\mathrm{abs1}}}{\partial t}+\frac{1}{12\eta}\,\nabla\cdot\left[h_0^3\nabla(P_{\mathrm{abs0}}P_{\mathrm{abs1}})\right]=P_{\mathrm{abs0}}\frac{\partial h_1}{\partial t}-\frac{1}{8\eta}\,\nabla\cdot\left[h_0^2h_1\nabla\left(P_{\mathrm{abs0}}^2\right)\right] \quad (8)$$

The above equations show that the dynamic pressure and its rate of change are coupled with the air film gap and its rate of change (the squeeze motion speed). The thrust of the air film on the air-floating surface is obtained by the pressure integral, so the spatial distribution of the corresponding air film pressure cannot be obtained by only specifying the dynamic force; that is, the characteristics of the air film can only be analyzed via the flexibility method: firstly, we specify the displacement form on the air film, and then solve the pressure change. Suppose that h_1 changes periodically in the following form:

$$h_1=\mathrm{Re}(\tilde{h}_1e^{j\omega t})=\mathrm{Re}\left[(h_{1\mathrm{c}}+jh_{1\mathrm{s}})e^{j\omega t}\right]=h_{1\mathrm{c}}\cos(\omega t)-h_{1\mathrm{s}}\sin(\omega t) \quad (9)$$

$$\frac{\mathrm{d}h_1}{\mathrm{d}t}=\mathrm{Re}(j\omega\tilde{h}_1e^{j\omega t})=-\omega[h_{1\mathrm{c}}\sin(\omega t)+h_{1\mathrm{s}}\cos(\omega t)] \quad (10)$$

For notation convenience, the real part is omitted, and a single-frequency vibration is directly expressed in the form of a complex exponential. The wavy line indicates a complex variable. The pressure distribution $P_{\mathrm{abs1}}(x,y,t)$ produces a corresponding periodic variation:

$$P_{\mathrm{abs1}}=\mathrm{Re}(\tilde{P}_1e^{j\omega t})=\mathrm{Re}\left[(P_{1\mathrm{c}}+jP_{1\mathrm{s}})e^{j\omega t}\right]=P_{1\mathrm{c}}\cos(\omega t)-P_{1\mathrm{s}}\sin(\omega t) \quad (11)$$

$$\frac{\partial P_{\mathrm{abs1}}}{\partial t}=\mathrm{Re}(j\omega\tilde{P}_1e^{j\omega t})=-\omega[P_{1\mathrm{c}}\sin(\omega t)+P_{1\mathrm{s}}\cos(\omega t)] \quad (12)$$

By bringing the complex expressions of displacement and pressure into Equation (7), the complex form of the perturbation Reynolds equation is obtained [35]:

$$2\,\nabla\cdot\left[h_0^3\nabla\left(P_{\mathrm{abs0}}\tilde{P}_1\right)\right]+3\,\nabla\cdot\left[h_0^2\tilde{h}_1\nabla\left(P_{\mathrm{abs0}}^2\right)\right]=24\eta\left(j\omega h_0\tilde{P}_1+j\omega P_{\mathrm{abs0}}\tilde{h}_1\right) \quad (13)$$

In fact, the above equation can be obtained by performing Laplace transformation on Equation (7) and letting $s=j\omega$. By using the flexibility method to determine the characteristics of the gas film, the form of displacement can arbitrarily specified. Therefore, let $h_{1\mathrm{c}}=0$, and we have $h_1=\mathrm{Re}\left[jh_{1\mathrm{s}}e^{j\omega t}\right]=-h_{1\mathrm{s}}\sin(\omega t)$, $P_{\mathrm{abs1}}=\mathrm{Re}\left[(P_{1\mathrm{c}}+jP_{1\mathrm{s}})e^{j\omega t}\right]$, Thereby,

$$2\,\nabla\cdot\left[h_0^3\nabla(P_{\mathrm{abs0}}P_{1\mathrm{s}})\right]-24\eta\omega h_0P_{1\mathrm{c}}=-3\,\nabla\cdot\left[h_0^2h_{1\mathrm{s}}\nabla\left(P_{\mathrm{abs0}}^2\right)\right] \quad (14)$$

$$12\eta\omega h_0P_{1\mathrm{s}}+\nabla\cdot\left[h_0^3\nabla(P_{\mathrm{abs0}}P_{1\mathrm{c}})\right]=-12\eta\omega P_{\mathrm{abs0}}h_{1\mathrm{s}} \quad (15)$$

The above equations and Equation (13) indicate that the real part and imaginary part of the dynamic pressure are mutually coupled; the amplitude of dynamic pressure $P_{\mathrm{abs1}}(x,y,t)$ is proportional to the forced displacement amplitude h_1. However, the phase of dynamic pressure has a nonlinear relationship with forced displacement frequency ω.

2.3. Stiffness and Damping of the Gas Film

Regardless of the influence of the fluid–solid coupling effect, the sides of the thin film are treated as a single rigid body, and a transfer function is used to describe the dynamic

characteristics of the bearing. In this kind of model, the plates composing lubricating film move as one. When the bearing is in translation, $\frac{\partial h_1}{\partial x} = \frac{\partial h_1}{\partial y} = 0$; therefore, h_1 in Equation (7) can be written outside the brackets, namely

$$2\,\nabla\cdot\left[h_0^3\nabla(P_{\text{abs0}}P_{\text{abs1}})\right] + 3h_1\,\nabla\cdot\left[h_0^2\nabla\left(P_{\text{abs0}}^2\right)\right] = 24\eta\left(h_0\frac{\partial P_{\text{abs1}}}{\partial t} + P_{\text{abs0}}\frac{\mathrm{d}h_1}{\mathrm{d}t}\right) \tag{16}$$

Equation (13) then changes to

$$2\,\nabla\cdot\left[h_0^3\nabla\left(P_{\text{abs0}}\tilde{P}_1\right)\right] + 3\tilde{h}_1\,\nabla\cdot\left[h_0^2\nabla\left(P_{\text{abs0}}^2\right)\right] = 24\eta\left(j\omega h_0\tilde{P}_1 + j\omega P_{\text{abs0}}\tilde{h}_1\right) \tag{17}$$

and Equation (14) changes to

$$2\,\nabla\cdot\left[h_0^3\nabla(P_{\text{abs0}}P_{1\text{s}})\right] - 24\eta\omega h_0 P_{1\text{c}} = -3\,\nabla\cdot\left[h_0^2\nabla\left(P_{\text{abs0}}^2\right)\right]h_{1\text{s}} \tag{18}$$

$$12\eta\omega h_0 P_{1\text{s}} + \nabla\cdot\left[h_0^3\nabla(P_{\text{abs0}}P_{1\text{c}})\right] = -12\eta\omega P_{\text{abs0}}h_{1\text{s}} \tag{19}$$

The dynamic stiffness of the gas film is defined as follows (note that the positive and negative of the calculation formula are related to the definition of the displacement direction, a sign of the real part and imaginary part of the dynamic pressure):

$$\begin{aligned} K_b(\omega) &= K(\omega) + j\omega C(\omega) = -\frac{\tilde{W}_1\mathrm{d}\Omega}{\tilde{h}_1} = -\frac{\iint_\Omega \tilde{P}_1\mathrm{d}\Omega}{\tilde{h}_1} \\ &= -\left[\frac{\iint_\Omega P_{1\text{c}}\mathrm{d}\Omega\cdot h_{1\text{c}} + \iint_\Omega P_{1\text{s}}\mathrm{d}\Omega\cdot h_{1\text{s}}}{h_{1\text{c}}^2 + h_{1\text{s}}^2} + j\omega\frac{\iint_\Omega P_{1\text{s}}\mathrm{d}\Omega\cdot h_{1\text{c}} - \iint_\Omega P_{1\text{c}}\mathrm{d}\Omega\cdot h_{1\text{s}}}{\omega(h_{1\text{c}}^2 + h_{1\text{s}}^2)}\right] \end{aligned} \tag{20}$$

Obviously, the calculation of dynamic stiffness from the above formula is complicated. When forcing a periodically varying displacement is $-h_{1\text{s}}\sin(\omega t)$ by making $h_{1\text{c}} = 0$, the formulas for calculating the dynamic stiffness and damping of the air film are as follows:

$$K(\omega) = -\frac{\iint_\Omega P_{1\text{s}}\mathrm{d}\Omega}{h_{1\text{s}}},\quad C(\omega) = \frac{\iint_\Omega P_{1\text{c}}\mathrm{d}\Omega}{\omega h_{1\text{s}}} \tag{21}$$

3. Analytical Results with Same Pressure Boundaries

3.1. A One-Dimensional Infinite Width Flat Air Film

Figure 1a shows a one-dimensional infinitely wide flat lubricating film. The gas film is surrounded by ambient pressure, which means that only two flat plates that are close to each other form a thin film in the air, and there is no flow when the upper plate does not move.

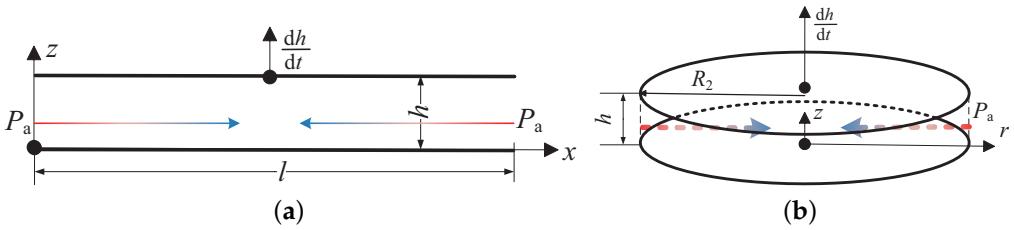

Figure 1. Squeeze film of the one-dimensional constant gap flow model: (**a**) infinite width flat air film; and (**b**) circular air film.

When fluid compressibility is considered, the dynamic Reynolds equation of the one-dimensional lubricating film in the Cartesian coordinate system is obtained from Equation (2):

$$h^3\frac{\mathrm{d}^2P_{\text{abs}}^2}{\mathrm{d}x^2} = 24\eta\frac{\mathrm{d}(hP_{\text{abs}})}{\mathrm{d}t} \tag{22}$$

By substituting the perturbation form in Equation (6) and the complex form in Equation (9), Equation (17) under the condition of a one-dimensional flat gas film is obtained:

$$\frac{\mathrm{d}^2(P_{\mathrm{abs0}}\tilde{P}_1)}{\mathrm{d}x^2}+\frac{3}{2}\frac{\tilde{h}_1}{h_0}\frac{\mathrm{d}^2(P_{\mathrm{abs0}}^2)}{\mathrm{d}x^2}=\frac{12\eta j\omega}{h_0^2}\tilde{P}_1+\frac{12\eta j\omega P_{\mathrm{abs0}}}{h_0^3}\tilde{h}_1 \tag{23}$$

When there is no high-pressure gas supply at the boundary, that is, the atmospheric pressure boundary, the steady-state pressure distribution is $P_{\mathrm{abs0}}(x)=P_{\mathrm{a}}$, which further simplifies Equation (23) with boundary conditions:

$$\frac{\mathrm{d}^2(\tilde{P}_1)}{\mathrm{d}x^2}=\frac{12\eta j\omega}{P_{\mathrm{a}}h_0^2}\tilde{P}_1+\frac{12\eta j\omega}{h_0^3}\tilde{h}_1,\ \ \tilde{P}_1(0)=0,\ \ \tilde{P}_1(l)=0,\ \ \frac{\mathrm{d}\tilde{P}_1}{\mathrm{d}x}\left(\frac{l}{2}\right)=0 \tag{24}$$

The analytical solution to this differential equation is:

$$\tilde{P}_1(x)=P_{\mathrm{a}}\frac{\tilde{h}_1}{h_0}\left[\frac{\cosh[\sqrt{\sigma_{\mathrm{s}}}e^{j\pi/4}(\frac{x}{l}-\frac{1}{2})]}{\cosh(\sqrt{\sigma_{\mathrm{s}}}e^{j\pi/4}\frac{1}{2})}-1\right],\ \ \sigma_{\mathrm{s}}=\frac{12\eta\omega l^2}{P_{\mathrm{a}}h_0^2} \tag{25}$$

where σ_{s} is the squeeze number. The expanded expression is as follows:

$$\begin{aligned}
P_{1\mathrm{s}}(x^*)&=\frac{2}{\cosh k+\cos k}\left(\cosh\frac{k}{2}\cos\frac{k}{2}\cosh kx^*\cos kx^*+\sinh\frac{k}{2}\sin\frac{k}{2}\sinh kx^*\sin kx^*\right)-1\\
P_{1\mathrm{c}}(x^*)&=\frac{2}{\cosh k+\cos k}\left(\sinh\frac{k}{2}\sin\frac{k}{2}\cosh kx^*\cos kx^*-\cosh\frac{k}{2}\cos\frac{k}{2}\sinh kx^*\sin kx^*\right)\\
\text{and,}\quad x^*&=\frac{x}{l}-\frac{1}{2},\quad k=\sqrt{\frac{\sigma_{\mathrm{s}}}{2}}
\end{aligned} \tag{26}$$

Figures 2 and 3 show the distribution of the dynamic pressure of a one-dimensional flat lubricating film under different compression numbers (no external air supply; only an atmospheric pressure boundary). Figure 2 shows a schematic diagram of the distribution of the pressure $P_{1\mathrm{s}}$ in the same phase with external excitation, which produces dynamic stiffness. Figure 3 shows a schematic diagram of the 90-degree-phase pressure distribution $P_{1\mathrm{c}}$, which produces damping. Since the boundary condition is a constant pressure, the dynamic pressure at the boundary is zero; thus, intuitively, the compressibility of the gas causes some of it to be trapped in the central area, and it cannot be removed and inhaled in time.

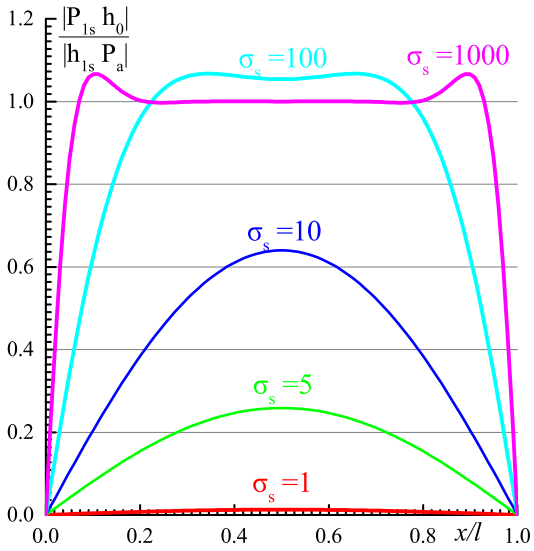

Figure 2. Distribution of $P_{1\mathrm{s}}$ inside of the 1D parallel slider.

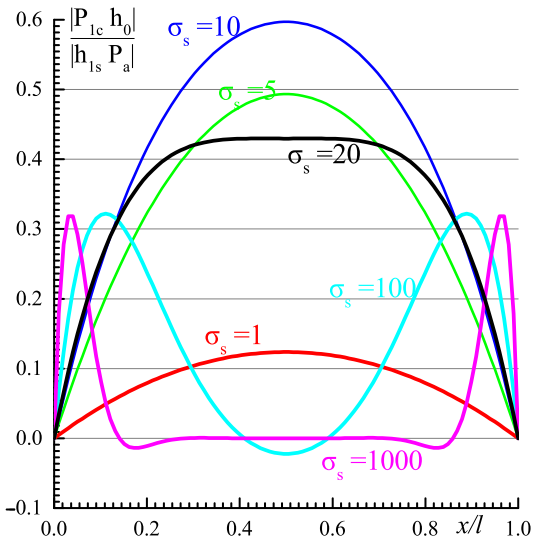

Figure 3. Distribution of P_{1c} inside the 1D parallel slider.

The definition of the dynamic stiffness Equation (20) can be used to obtain the dimensionless dynamic stiffness and damping expressions of the air film:

$$K^*(\omega) = \frac{K(\omega)}{blP_a/h_0} = \mathrm{Re}\left[1 - 2\frac{\tanh\left(\sqrt{\sigma_s}e^{j\pi/4}/2\right)}{\sqrt{\sigma_s}e^{j\pi/4}}\right] = 1 - \frac{1}{k}\frac{\sinh k + \sin k}{\cosh k + \cos k} \tag{27}$$

$$C^*(\omega) = \frac{C(\omega)}{\eta bl^3/h_0^3} = \frac{12}{\sigma_s}\mathrm{Im}\left[1 - 2\frac{\tanh\left(\sqrt{\sigma_s}e^{j\pi/4}/2\right)}{\sqrt{\sigma_s}e^{j\pi/4}}\right] = \frac{12}{\sigma_s}\frac{1}{k}\frac{\sinh k - \sin k}{\cosh k + \cos k} \tag{28}$$

Figure 4 shows the variation in the dimensionless dynamic stiffness and the damping coefficient with the squeeze number. It is known that the dynamic coefficients of the incompressible fluid lubricating film are all constant, the stiffness is zero, and the damping is constant. As a comparison, the dynamic coefficient of the compressible gas film varies with the excitation frequency: when the excitation frequency is $\omega \to 0$, the squeeze number $\sigma_s \to 0$, and the gas film behaves like the incompressible lubricating film; with the excitation frequency increasing, the squeeze number increases, and when $\sigma_s > 100$, the air film only shows rigidity, and the damping is almost negligible.

As shown in Figure 5, the dynamic stiffness amplitude varies with the squeeze number: as the squeeze number increases, the dynamic coefficient of the incompressible fluid lubricating film increases linearly, but when the squeeze number $\sigma_s > 10$, the dynamic stiffness amplitude of the air film no longer increases, and the dimensionless number approaches the limit 1. With the increase in the squeeze number, the rigid restoring force of the air film increases, but the damping force decreases. The frequency with the same amplitude is called the cutoff frequency. For a one-dimensional flat plate on the atmospheric boundary, the squeeze number corresponding to the crossover frequency is approximately 10.

The above analysis shows that whether the squeeze film exhibits damping or rigidity depends on the size of the squeeze number, and the squeeze number, i.e., $\sigma_s = 674.5$ based on Table 1, is calculated according to Equation (25). It can be seen that, since the gap of the bearing is small, the stiffness effect produced by the squeeze film is relatively large. When analyzing the dynamic characteristics of the bearing, the squeeze film effect must be considered.

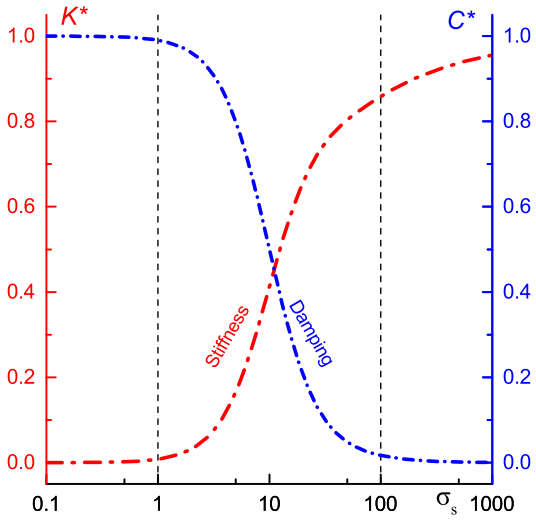

Figure 4. Dynamic coefficients of the 1D parallel slider.

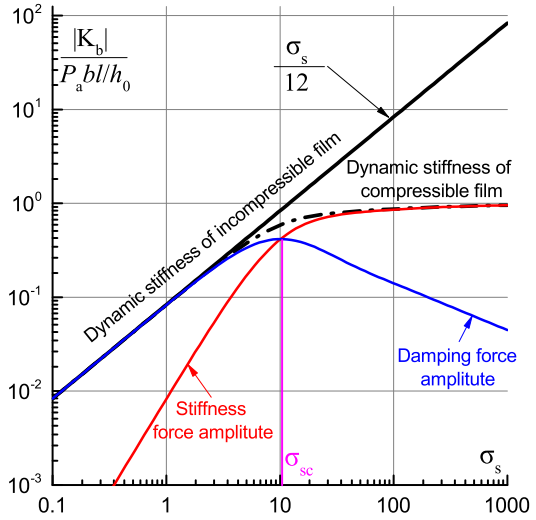

Figure 5. Dynamic stiffness modulus of the 1D parallel slider.

Table 1. Parameters of a typical aerostatic guideway.

Name	Viscosity	Disturbance Frequency	Characteristic Length	Film Thickness
Value	17.9×10^{-6} Pa · s	500 Hz	0.1 m	10×10^{-6} m

3.2. One-Dimensional Circular Air Film

As shown in Figure 1b, the normal movement of a gas film is superimposed on the basis of a circular plate gas film. When fluid compressibility is considered, the dynamic Reynolds equation of the one-dimensional lubricating film in the cylindrical coordinate system is obtained from Equation (3):

$$\frac{1}{r}\frac{\partial}{\partial r}\left(\frac{h^3}{12\eta} r P_{\text{abs}} \frac{\partial P_{\text{abs}}}{\partial r}\right) = \frac{\partial (h P_{\text{abs}})}{\partial t} \tag{29}$$

By substituting the perturbation form in Equation (6) and the complex form in Equation (9), the form of Equation (17) inside of a one-dimensional annular flat plate gas film is:

$$\frac{\mathrm{d}}{\mathrm{d}r}\left(\frac{\mathrm{d}(P_{\mathrm{abs0}}\tilde{P}_1)}{\mathrm{d}r}+\frac{3}{2}\frac{\tilde{h}_1}{h_0}\frac{\mathrm{d}P_{\mathrm{abs0}}^2}{\mathrm{d}r}\right)+\frac{1}{r}\left(\frac{\mathrm{d}(P_{\mathrm{abs0}}\tilde{P}_1)}{\mathrm{d}r}+\frac{3}{2}\frac{\tilde{h}_1}{h_0}\frac{\mathrm{d}P_{\mathrm{abs0}}^2}{\mathrm{d}r}\right)=\frac{12\eta j\omega}{h_0^2}\tilde{P}_1+\frac{12\eta j\omega P_{\mathrm{abs0}}}{h_0^3}\tilde{h}_1 \tag{30}$$

The solution without supply pressure (the atmospheric pressure boundary) will now be discussed. Under this condition, the steady-state pressure distribution is $P_{\mathrm{abs0}}(r)=P_{\mathrm{a}}$, That is, Equation (30) is further simplified, and there are boundary conditions (the inner hole radius is equal to zero):

$$\frac{\mathrm{d}^2\tilde{P}_1}{\mathrm{d}r^2}+\frac{1}{r}\frac{\mathrm{d}\tilde{P}_1}{\mathrm{d}r}=\frac{12\eta}{P_{\mathrm{a}}h_0^2}j\omega\tilde{P}_1+\frac{12\eta}{h_0^3}j\omega\tilde{h}_1,\ \ \tilde{P}_1(R_2)=0,\ \ \frac{\mathrm{d}\tilde{P}_1}{\mathrm{d}r}(0)=0 \tag{31}$$

The analytical solution to this differential equation is:

$$\tilde{P}_1(r)=P_{\mathrm{a}}\frac{\tilde{h}_1}{h_0}\left(\frac{J_0(\sqrt{\sigma_{\mathrm{s}}}e^{j\pi/4}r^*)}{J_0(\sqrt{\sigma_{\mathrm{s}}}e^{j\pi/4})}-1\right),\ \ \sigma_{\mathrm{s}}=\frac{12\eta\omega R_2^2}{P_{\mathrm{a}}h_0^2},\ \ r^*=\frac{r}{R_2} \tag{32}$$

The expanded expression is as follows:

$$\begin{aligned}P_{1\mathrm{s}}(r^*)&=\frac{\mathrm{ber}\,\sqrt{\sigma_{\mathrm{s}}}\,\mathrm{ber}\,(\sqrt{\sigma_{\mathrm{s}}}r^*)+\,\mathrm{bei}\,\sqrt{\sigma_{\mathrm{s}}}\,\mathrm{bei}\,(\sqrt{\sigma_{\mathrm{s}}}r^*)}{(\,\mathrm{ber}\,\sqrt{\sigma_{\mathrm{s}}})^2+(\,\mathrm{bei}\,\sqrt{\sigma_{\mathrm{s}}})^2}-1\\ P_{1\mathrm{c}}(r^*)&=\frac{\mathrm{bei}\,\sqrt{\sigma_{\mathrm{s}}}\,\mathrm{ber}\,(\sqrt{\sigma_{\mathrm{s}}}r^*)-\,\mathrm{ber}\,\sqrt{\sigma_{\mathrm{s}}}\,\mathrm{bei}\,(\sqrt{\sigma_{\mathrm{s}}}r^*)}{(\,\mathrm{ber}\,\sqrt{\sigma_{\mathrm{s}}})^2+(\,\mathrm{bei}\,\sqrt{\sigma_{\mathrm{s}}})^2}\end{aligned} \tag{33}$$

In applied mathematics, the Kelvin functions $\mathrm{ber}_\nu(x)$ and $\mathrm{bei}_\nu(x)$ are the real and imaginary parts, respectively, of $J_\nu\left(xe^{\frac{3\pi i}{4}}\right)$, where x is real, and $J_\nu(z)$ is the ν^{th} order Bessel function of the first kind.

The definition of the dynamic stiffness of the air film, as given in Equation (20), can be used to obtain the dynamic stiffness and damping expressions of the air film:

$$\begin{aligned}K^*(\omega)&=\frac{K(\omega)}{\pi R_2^2P_{\mathrm{a}}/h_0}=\mathrm{Re}\left[1-2\frac{J_1(\sqrt{\sigma_{\mathrm{s}}}e^{j\pi/4})}{\sqrt{\sigma_{\mathrm{s}}}e^{j\pi/4}J_0(\sqrt{\sigma_{\mathrm{s}}}e^{j\pi/4})}\right]\\ &=1-\sqrt{\frac{2}{\sigma_{\mathrm{s}}}}\frac{\mathrm{ber}\,\sqrt{\sigma_{\mathrm{s}}}(\mathrm{bei}_1\sqrt{\sigma_{\mathrm{s}}}-\mathrm{ber}_1\sqrt{\sigma_{\mathrm{s}}})-\,\mathrm{bei}\,\sqrt{\sigma_{\mathrm{s}}}(\mathrm{ber}_1\sqrt{\sigma_{\mathrm{s}}}+\mathrm{bei}_1\sqrt{\sigma_{\mathrm{s}}})}{(\mathrm{ber}\sqrt{\sigma_{\mathrm{s}}})^2+(\mathrm{bei}\sqrt{\sigma_{\mathrm{s}}})^2}\end{aligned} \tag{34}$$

$$\begin{aligned}C^*(\omega)&=\frac{C(\omega)}{\eta\pi R_2^4/h_0^3}=\frac{12}{\sigma_{\mathrm{s}}}\,\mathrm{Im}\left[2\frac{J_1(\sqrt{\sigma_{\mathrm{s}}}e^{j\pi/4})}{\sqrt{\sigma_{\mathrm{s}}}e^{j\pi/4}J_0(\sqrt{\sigma_{\mathrm{s}}}e^{j\pi/4})}-1\right]\\ &=\sqrt{\frac{2}{\sigma_{\mathrm{s}}}}\frac{\mathrm{ber}\,\sqrt{\sigma_{\mathrm{s}}}(\mathrm{ber}_1\sqrt{\sigma_{\mathrm{s}}}+\mathrm{bei}_1\sqrt{\sigma_{\mathrm{s}}})-\,\mathrm{bei}\,\sqrt{\sigma_{\mathrm{s}}}(\mathrm{bei}_1\sqrt{\sigma_{\mathrm{s}}}-\mathrm{ber}_1\sqrt{\sigma_{\mathrm{s}}})}{(\mathrm{ber}\sqrt{\sigma_{\mathrm{s}}})^2+(\mathrm{bei}\sqrt{\sigma_{\mathrm{s}}})^2}\end{aligned} \tag{35}$$

Figure 6 shows the changing trend of the dimensionless dynamic stiffness and damping coefficient with the squeeze number, and Figure 7 shows the dynamic stiffness amplitude with the squeeze number. Obviously, the squeeze film characteristics of the parallel circular plate and flat lubricating film are similar, but the dimensionless damping at zero frequency becomes 1.5 (this is consistent with the damping obtained when compressibility is not considered), and then the crossover frequency shifts to the left. The squeeze number corresponding to the crossover frequency is approximately equal to $\sigma_{\mathrm{sc}}\approx 6$.

Similarly to a guide railway, by substituting Equation (32), the squeeze number of the common thrust bearing air film shown in Table 2 is estimated $\sigma_{\mathrm{s}}=168.6$. Since the clearance of the bearing is small, the stiffness effect of the squeeze film is relatively large. The result of the above formula shows that the squeeze film effect must be considered when analyzing the dynamic characteristics of the thrust bearing.

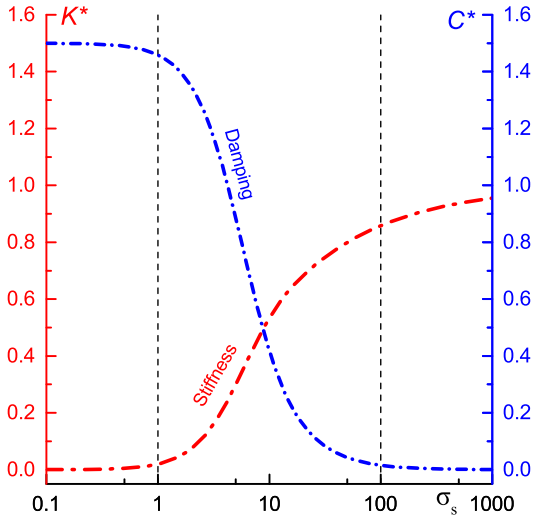

Figure 6. Dynamic coefficients of the 1D parallel disc.

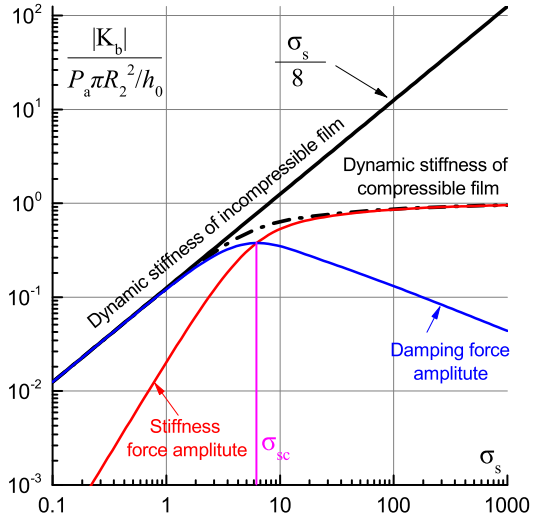

Figure 7. Dynamic stiffness modulus of the 1D parallel disc.

Table 2. Parameters of a typical aerostatic thrust bearing.

Name	Viscosity	Disturbance Frequency	Characteristic Radius	Film Thickness
Value	17.9×10^{-6} Pa · s	500 Hz	0.05 m	10×10^{-6} m

4. Numerical Results with Different Pressure Boundaries

The static and perturbation Reynolds equations are all elliptic differential equations without time, so they can be conveniently solved by the FEM. With the development of modern computing technology, the related literature has increased, so the basic theory of the FEM and the Reynolds equation solving process adopting FEM will not be expanded upon in detail here. The interested reader can refer to [36,37].

The static characteristics of the aerostatic bearing and the dynamic characteristics are evaluated considering the stiffness and damping coefficients. The flowchart for solving the Reynolds equation is shown in Figure 8. Firstly, the steady-state Reynolds equation is solved and the static performance is determined. Secondly, the coupled perturbation Reynolds equations are solved to obtain the dynamic performances of the air bearing.

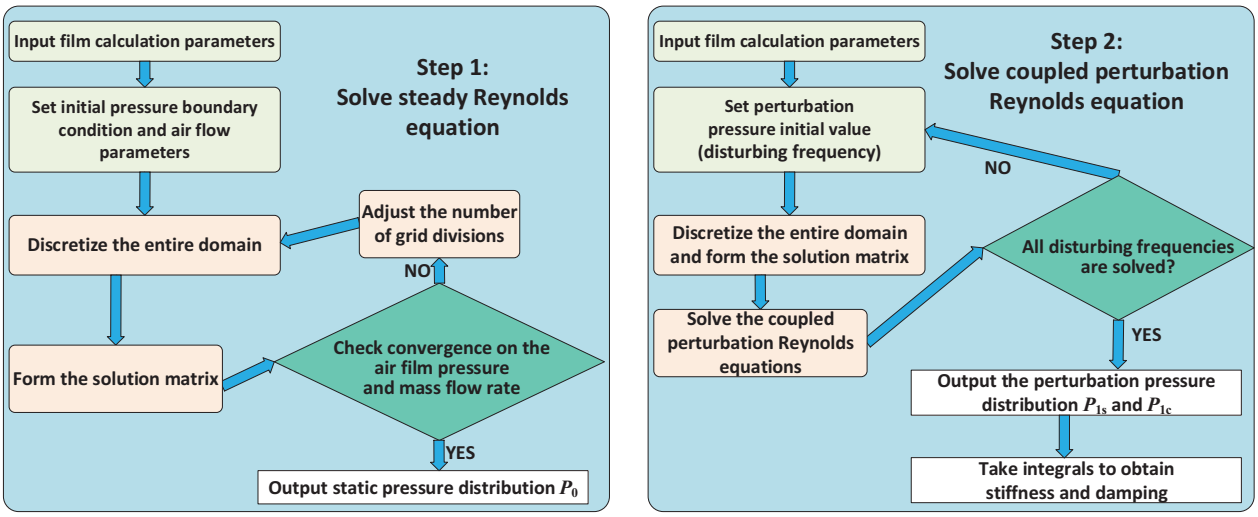

Figure 8. Flowchart of the calculation procedure.

4.1. A One-Dimensional Infinite Width Flat Air Film

The first example of a numerical solution to the perturbed Reynolds equation is as follows: The dynamic characteristics in the flat plate with external pressure equal gap as shown in Figure 9a are calculated. For the one-dimensional flat lubricating film shown in Figure 9a, when compressibility is considered, the steady-state pressure distribution is determined by Equation (2), and the dynamic pressure distribution is determined by Equation (23). In order to make the results more universal, the following variable substitutions are used:

$$P_{\mathrm{abs0}} = P^*_{\mathrm{abs0}} P_{\mathrm{a}},\ P_{\mathrm{d}} = P_{\mathrm{a}}/\sigma,\ \tilde{P}_1 = \tilde{P}^*_1 P_{\mathrm{a}},\ \tilde{h}_1 = \tilde{h}^*_1 h_0,\ x = x^* l,\ \sigma_{\mathrm{s}} = \frac{12\eta\omega l^2}{P_{\mathrm{a}} h_0^2} \tag{36}$$

where σ is the reciprocal of dimensionless air supply pressure. The dimensionless Equation (23) is as follows:

$$\frac{\mathrm{d}^2(P^*_{\mathrm{abs0}}\tilde{P}^*_1)}{\mathrm{d}x^{*2}} + \frac{3}{2}\tilde{h}^*_1 \frac{\mathrm{d}^2(P^{*2}_{\mathrm{abs0}})}{\mathrm{d}x^{*2}} = j\sigma_{\mathrm{s}}\tilde{P}^*_1 + j\sigma_{\mathrm{s}} P^*_{\mathrm{abs0}}\tilde{h}^*_1,\ \ P^*_{\mathrm{abs0}} = P^*_{\mathrm{abs0}}(\sigma, x^*) \tag{37}$$

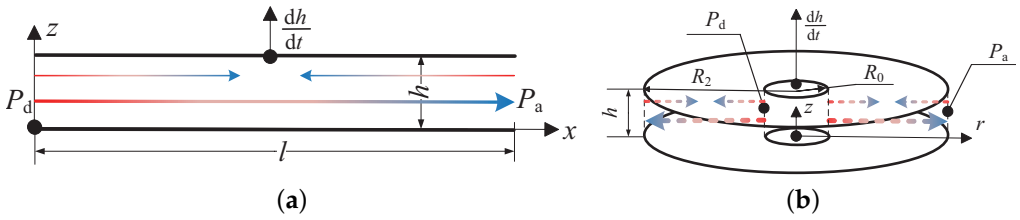

Figure 9. Squeeze film of a one-dimensional constant gap flow model with different pressure boundaries: (**a**) infinite width flat air film; and (**b**) circular air film.

The above dimensionless form shows that we only need to solve for different supply pressure ratios and squeeze numbers to fully understand the dynamic characteristics of one-dimensional flat films. The FEM was used to solve the above equations. Figures 10 and 11 are the real part $P_{1\mathrm{s}}$ and imaginary part $P_{1\mathrm{c}}$ of the dynamic pressure distribution with different air supply pressures σ and different squeeze numbers σ_{s}. It can be seen from those figures that, as the gas supply pressure increases, the high pressure area of the dynamic pressure is also shifted to the left, where more gas is compressed and concentrated, since the high-pressure area in the steady-state pressure distribution is near the origin of the x axis.

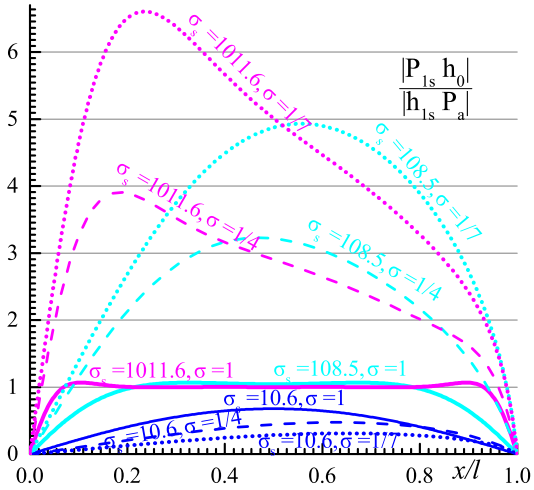

Figure 10. Distribution of P_{1s} inside of the 1D parallel slider with high-pressure in the left.

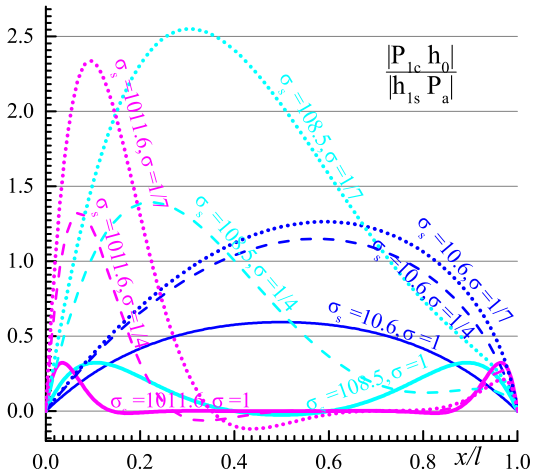

Figure 11. Distribution of P_{1c} inside of 1D parallel slider with high-pressure in the left.

Integrating the real and imaginary parts of the dynamic pressure, Figure 12 shows the dimensionless dynamic stiffness and damping coefficient of the one-dimensional flat plate with a gas supply boundary, and its definition is the same as that under the atmospheric pressure gas supply boundary in Equation (27). Because the air supply pressure is greater than the atmospheric pressure, the value of the dimensionless dynamic stiffness is greater than 1. The maximum value of stiffness can be seen to increase from 1 to 6 when the supplying pressure changes from zero to 9 bar. As a comparison, the dimensionless dynamic stiffness in Figure 4 is always less than 1.

Improving the supply pressure does not improve the amplitude of the damping coefficient, but delays its decreasing frequency. It can be seen in Figure 12 that the half-damping squeeze number is increasing from 10 to 70 when the supplying pressure changes from 0 to 9 bar. It is somewhat strange that the value of stiffness is decreasing with the improvement in the supply pressure in the low-frequency region. The effects of the increasing damping and the decreasing stiffness together increase the cut-off frequency from 10 to 70 with an increase in supply pressure, as shown in Figure 13. Figure 13 clearly shows that the increase in the air supply pressure increases both the damping force and the stiffness force.

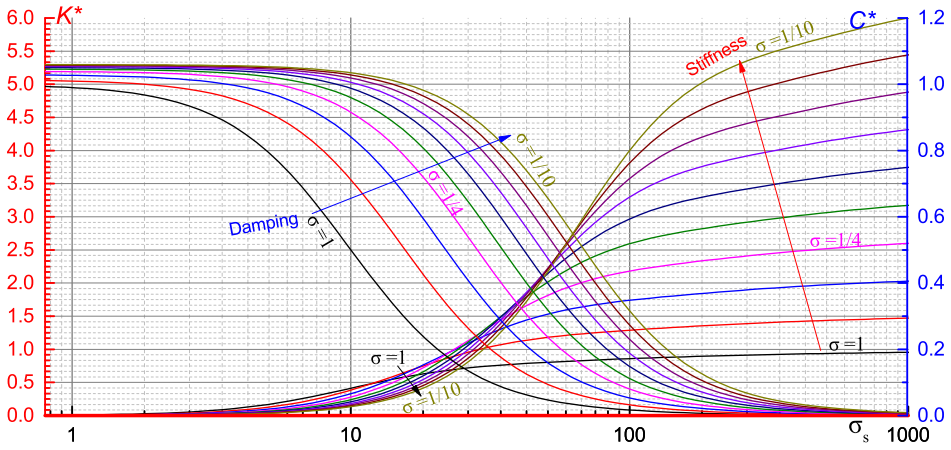

Figure 12. Dynamic coefficients of the 1D parallel slider with supply pressure.

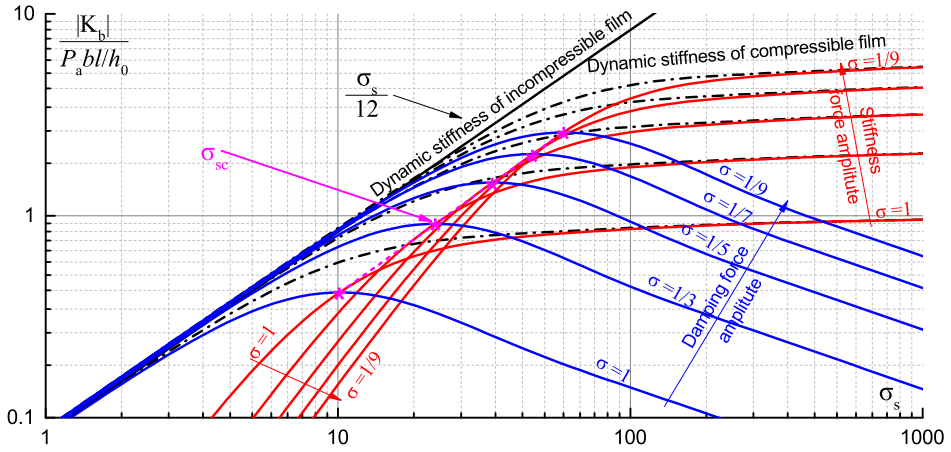

Figure 13. Dynamic stiffness modulus of the 1D parallel slider with supply pressure.

4.2. A One-Dimensional Annular Air Film Flowing from the Inside and the Outside

The second example of a numerical solution to the disturbed Reynolds equation is as follows: the one-dimensional flow model in cylindrical coordinate system shown in Figure 9b is calculated. Gas will flow from the inside to the outside if the inner diameter R_0 is of a high-pressure boundary and the outer diameter R_2 is of an atmospheric pressure boundary. In the same way, gas will flow from the outside to the inside if the outer diameter R_2 is of a supplying boundary. When considering gas compressibility, the steady-state pressure distribution of the one-dimensional annular lubricating film is determined by Equation (3), and the dynamic pressure distribution is determined by Equation (30). The following variable substitutions are used:

$$\begin{aligned} &P_{\mathrm{abs0}} = P^*_{\mathrm{abs0}} P_{\mathrm{a}},\ P_{\mathrm{d}} = P_{\mathrm{a}}/\sigma,\ \tilde{P}_1 = \tilde{P}^*_1 P_{\mathrm{a}},\ \tilde{h}_1 = \tilde{h}^*_1 h_0, \\ &r = r^* R_0,\ L'_2 = R_2/R_0,\ \sigma_{\mathrm{s}} = \frac{12\eta\omega(R_2 - R_0)^2}{P_{\mathrm{a}} h_0^2} \end{aligned} \tag{38}$$

where σ is the reciprocal of the dimensionless air supply pressure. The dimensionless Equation (30) is as follows:

$$\left(\frac{\mathrm{d}}{\mathrm{d}r^*} + \frac{1}{r^*}\right)\left(\frac{\mathrm{d}(P^*_{\mathrm{abs0}}\tilde{P}^*_1)}{\mathrm{d}r^*} + \frac{3}{2}\tilde{h}^*_1 \frac{\mathrm{d}P^{*2}_{\mathrm{abs0}}}{\mathrm{d}r^*}\right) = j\sigma_{\mathrm{s}}\tilde{P}^*_1 + j\sigma_{\mathrm{s}} P^*_{\mathrm{abs0}}\tilde{h}^*_1,\ \ P^*_{\mathrm{abs0}} = P^*_{\mathrm{abs0}}(\sigma, L'_2, r^*) \tag{39}$$

The above dimensionless form of P^*_{abs0} indicates that we need to analyze the dynamic characteristics of a one-dimensional ring squeeze film with different external and internal diameter ratios, supply pressure ratios, and squeeze numbers. Using the FEM to solve the above equations, the real part of the dynamic pressure P_{1s} and the imaginary part P_{1c} with different air supply pressures σ and different squeeze numbers σ_s (the ratio of outer and inner diameters $L'_2 = 1.5$) are illustrated in Figures 14 and 15, respectively. These figures show that more gas is compressed and concentrated close to the inner diameter with the increase in gas supply pressure, since the high-pressure area is located on the inner edge. The high-pressure area of the dynamic pressure also shifts to the inner diameter, which is similar to that of a one-dimensional flat plate.

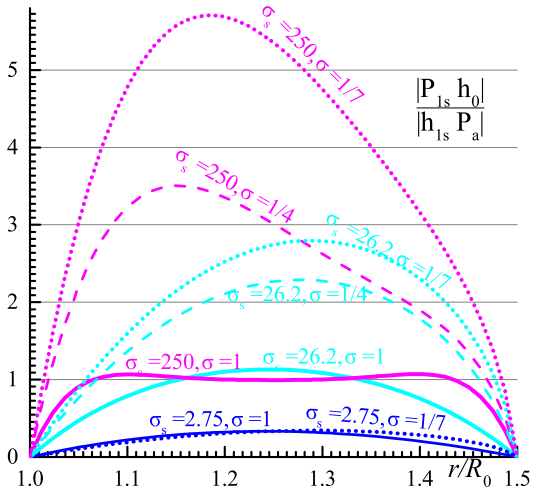

Figure 14. Distribution of P_{1s} inside of the 1D parallel ring with high-pressure inside.

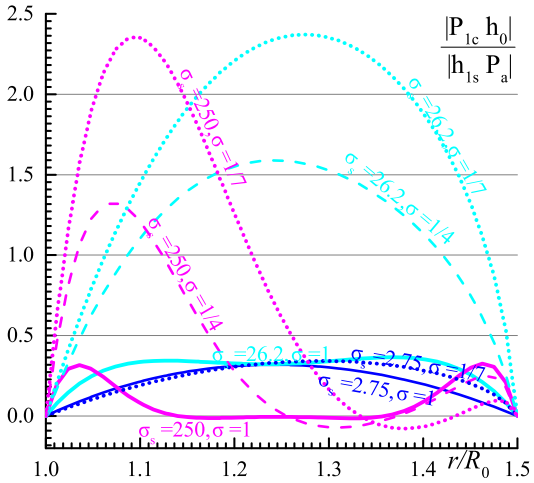

Figure 15. Distribution of P_{1c} inside of the 1D parallel ring with high-pressure inside.

The real part and imaginary part of the dynamic pressure are integrated to obtain the dimensionless dynamic stiffness and damping coefficient of the ring-type thin film, as shown in Figure 16, and its definition is similar to the definition under the atmospheric pressure gas supply boundary:

$$K^*(\omega) = \frac{K(\omega)}{\pi(R_2^2 - R_0^2)P_a/h_0}, \quad C^*(\omega) = \frac{C(\omega)}{\eta\pi(R_2^2 - R_0^2)(R_2 - R_0)^2/h_0^3} \tag{40}$$

Figure 16 shows the dynamic characteristic coefficient under different ratios of outer and inner diameters. It is noted that the dimensionless stiffness and damping ordinates in

the figures are exactly the same. With the increase in the ratio of outer and inner diameters, the maximum stiffness slightly decreases, and the damping coefficient remains almost unchanged, which shows that the dimensionless value is basically irrelevant to the ratio of inner and outer diameters, and indicates that the aforementioned dimensionless definition is appropriate.

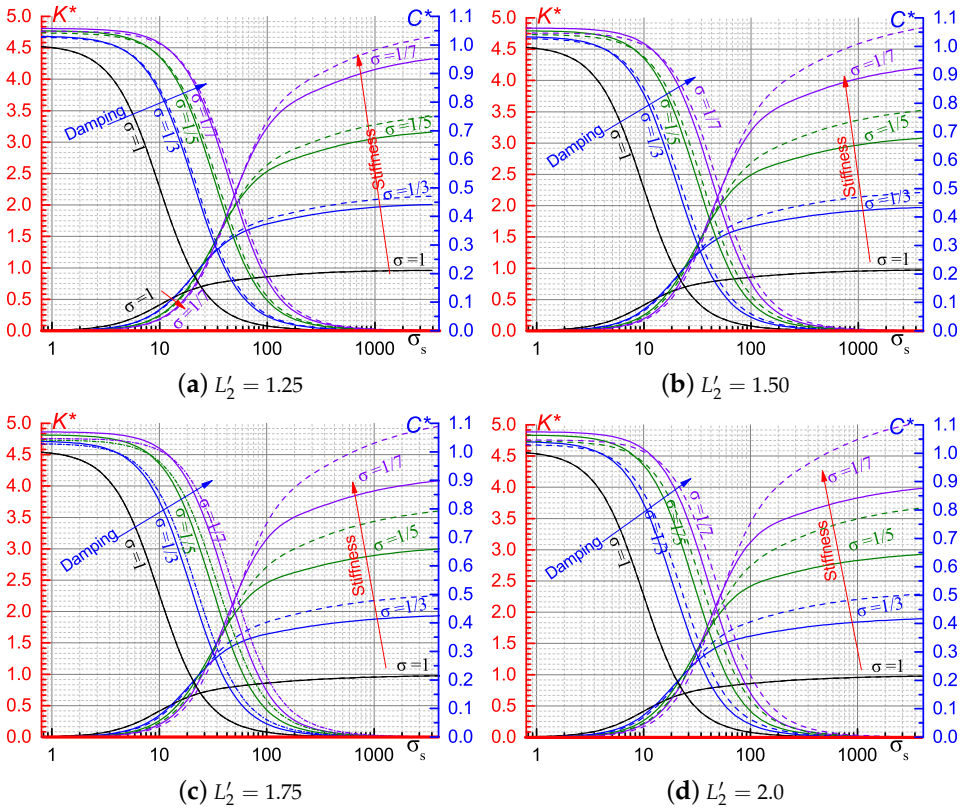

(**a**) $L_2' = 1.25$ (**b**) $L_2' = 1.50$

(**c**) $L_2' = 1.75$ (**d**) $L_2' = 2.0$

Figure 16. Dynamic coefficients of the 1D ring with supply pressure under different radius ratios.

By carefully analyzing the definition of the dimensionless damping coefficient in Equation (40), it is clear that, due to the roughly quadratic relationship between the reference value and the ratio of the outer and inner diameters R_2/R_0, the radius ratio is key in the design of thrust bearings.

The solid line in Figure 16 represents the result of the flow from inside to outside, and the dotted line represents the performance curve of the flow from outside to inside. As the disturbance frequency increases, the dimensionless stiffness of the flow from the outside is larger than that from the inside. The definition in Equation (44) shows that, under the same gap, the larger the area of the high pressure zone, the larger the load value obtained by integration, and the larger the value of the maximum stiffness. Obviously, the high-pressure boundary at the outer edge R_2 is larger than the high-pressure area at the inner edge R_0. Therefore, the flow direction has little effect on the damping coefficient, but as the radius ratio increases, the flow direction has a greater impact on the stiffness coefficient.

Because the air supply pressure is greater than the atmospheric pressure, the value of the dimensionless dynamic stiffness is greater than 1. It is clear that the maximum value of the stiffness increases from 1 to 5 when the supplying pressure changes from 0 to 6 bar. As a comparison, the dimensionless dynamic stiffness in Figure 6 is always less than 1.

Improving the supply pressure does not improve the amplitude of the damping coefficient, but it does delay its decreasing frequency. In the intermediate frequency region, the air supply pressure has a very strong influence on the damping (note that the abscissa is a logarithmic coordinate); it can be seen in Figure 16 that the half-damping squeeze

number is increasing from 10 to 70 when the supplying pressure changes from 0 to 9 bar. It is slightly strange that the value of the stiffness is decreasing with the improvement in the supply pressure in the low-frequency region. The effects of the increasing damping and decreasing stiffness together increase the cut-off frequency from 10 to 60 as the supply pressure increases, as shown in Figure 16. Figure 17 clearly shows that the increase in the air supply pressure increases both the damping force and the stiffness force.

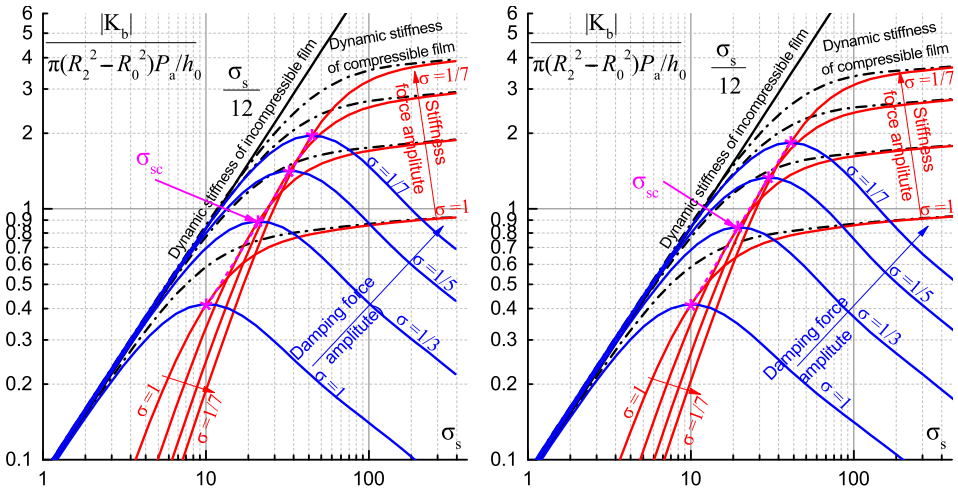

(**a**) $L_2' = 1.25$ (**b**) $L_2' = 2.0$

Figure 17. Dynamic stiffness modulus of the 1D ring with supply pressure under different radius ratios (flows from inside).

Figure 18 shows the dynamic stiffness modulus of the 1D ring with supply pressure under different radius ratios when the air flows in from outside. It can be seen that the flow direction does not cause much difference compared with Figure 16 when the air flows from inside.

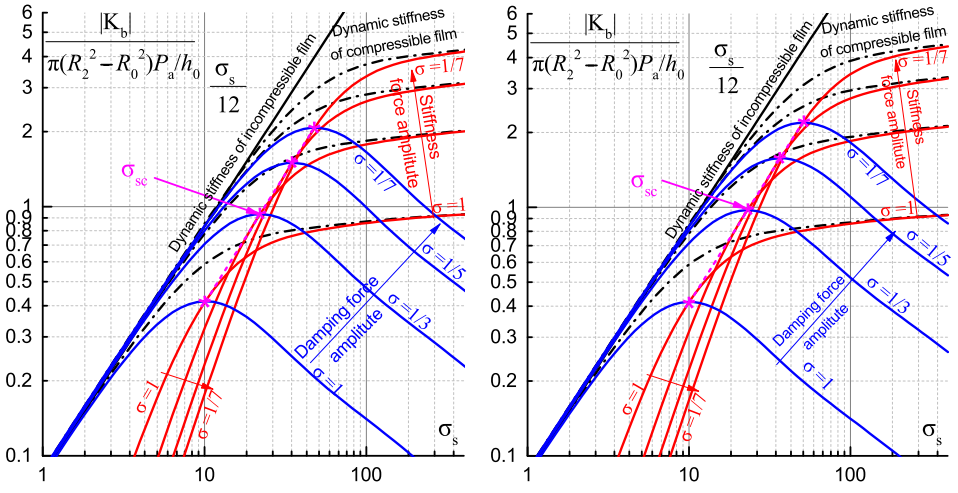

(**a**) $L_2' = 1.25$ (**b**) $L_2' = 2.0$

Figure 18. Dynamic stiffness modulus of the 1D ring with supply pressure under different radius ratios (flows from outside).

5. Results and Discussion

5.1. Characteristics of the Thin Film with Exciting Frequency Approaching Zero

Although the calculation results in Equation (16) show that the real and imaginary parts of the dynamic pressure are coupled, some basic conclusions can be drawn at low and high frequencies through limit analysis.

When the exciting frequency approaches zero $\omega \to 0$, Equation (16) can be simplified:

$$\boldsymbol{\nabla}\cdot\left[h_0^3\boldsymbol{\nabla}(P_{\text{abs0}}P_{1\text{s}})\right]+\frac{3}{2}h_{1\text{s}}\,\boldsymbol{\nabla}\cdot\left[h_0^2\boldsymbol{\nabla}\left(P_{\text{abs0}}^2\right)\right]=0,\quad P_{1\text{c}}\to 0 \tag{41}$$

Obviously, the first formula of the above equation is the solution formula of static stiffness. When the gap distribution is uniform, that is to say, h_0 is a constant, it can be simplified to obtain $P_{1\text{s}} = 0$ by combining with the Laplace Equation (4). Therefore, purely parallel plates have no static stiffness, regardless of whether the pressure boundary is uniform. It is clear that if the Laplace Equation (4) is completely unrelated to the translational gap h, the pressure distribution is also completely unrelated to that gap, so the bearing capacity is also completely unrelated to it, that is, there is no stiffness.

When there is no gradient in the static pressure distribution (no additional supply pressure), the simplification can also lead to $P_{1\text{s}} = 0$, the static stiffness of the parallel plate is 0, and there is only a certain squeeze film damping. However, when the frequency approaches 0, so does the disturbance velocity and the damping force.

The transposition of Equation (14) (b) leads to the following:

$$\boldsymbol{\nabla}\cdot\left[h_0^3\boldsymbol{\nabla}\left(P_{\text{abs0}}\frac{P_{1\text{c}}}{\omega h_{1\text{s}}}\right)\right]=-12\eta h_0\frac{P_{1\text{s}}}{h_{1\text{s}}}-12\eta P_{\text{abs0}} \tag{42}$$

It should therefore be noted that the damping coefficient (the damping force divided by the product of the frequency and amplitude) is not zero, and the gas then behaves like an incompressible liquid.

5.2. Characteristics of the Thin Film with an Exciting Frequency Approaching Infinity

When the vibration frequency approaches infinity $\omega \to +\infty$, Equation (16) is simplified:

$$P_{1\text{s}}=-P_{\text{abs0}}\frac{h_{1\text{s}}}{h_0},\quad P_{1\text{c}}=0 \tag{43}$$

At this time, the air film behaves like a rigid spring. The above formula shows that the ultimate stiffness coefficient of the bearing is related to the static (absolute) pressure distribution, and the damping is zero. By bringing the expression of the above formula $P_{1\text{s}}$ into the stiffness calculation Formula (21), we have

$$K_\infty=\iint_\Omega\frac{P_{\text{abs0}}}{h_0}\mathrm{d}\Omega=\frac{\iint_\Omega P_{\text{abs0}}\mathrm{d}\Omega}{h_0} \tag{44}$$

The above formula shows that K_∞ is only related to the static pressure distribution and gap distribution of the gas film, independently of other factors.

5.3. Transfer Function of the Thin Film

The above process shows that a correct analytical solution can be obtained by directly solving the perturbation Reynolds equation. However, the squeeze film effect of a compressible air film is complicated, and the expression of stiffness and damping are nonlinear functions of excitation frequency, which makes them difficult to apply directly. Therefore, using a certain simplified analysis to describe the dynamic characteristics of the air film simply by using several parameters would be highly beneficial for further design analysis.

Based on the characteristics of thin films with exciting frequencies approaching to zero and infinity, and observing the real and imaginary parts of the stiffness in

Figures 5, 7, 13, 17a,b and 18a,b, the air film stiffness can be represented by the transfer function shown below:

$$K_b(s) = -\frac{W_1(s)}{h_1(s)} = \frac{As}{\tau s + 1}, \quad K_b(j\omega) = \frac{\omega^2 A\tau}{\tau^2\omega^2 + 1} + j\omega\frac{A}{\tau^2\omega^2 + 1} \tag{45}$$

By substituting the values at frequencies of zero and infinity, the values of variables A and τ can be obtained:

$$A = C(0), \quad \tau = \frac{C(0)}{K(\infty)} \tag{46}$$

Table 3 shows the values of all the calculation results found. Since the damping at zero frequency is basically independent of the air supply pressure, and the air film stiffness is positively correlated with the air supply pressure at high frequencies, the time constant is negatively correlated with the air supply pressure.

Table 3. Parameters of a typical aerostatic thrust bearing.

Model	Boundary Setting	$A = C(0)$	$K(\infty)$	$\tau = C(0)/K(\infty)$
1D flat film	Ambient pressure	$\eta bl^3/(h_0^3)$	blP_a/h_0	$\eta l^2/(h_0^2 P_a)$
1D circular film	Ambient pressure	$3\eta\pi R_2^4/(2h_0^3)$	$\pi R_2^2 P_a/h_0$	$3\eta R_2^2/(2h_0^2 P_a)$
1D flat film	$\sigma_s = 1/3$	$1.028\eta bl^3/(h_0^3)$	$2.148blP_a/h_0$	$0.479\eta l^2/(h_0^2 P_a)$
1D flat film	$\sigma_s = 1/5$	$1.046\eta bl^3/(h_0^3)$	$3.393blP_a/h_0$	$0.414\eta l^2/(h_0^2 P_a)$
1D flat film	$\sigma_s = 1/7$	$1.054\eta bl^3/(h_0^3)$	$4.652blP_a/h_0$	$0.227\eta l^2/(h_0^2 P_a)$
1D flat film	$\sigma_s = 1/9$	$1.058\eta bl^3/(h_0^3)$	$5.911blP_a/h_0$	$0.179\eta l^2/(h_0^2 P_a)$
1D annular film	$\sigma_s = 1, L_2' = 1.25$	$\frac{\eta\pi(R_2^2-R_0^2)(R_2-R_0)^2}{h_0^3}$	$\frac{\pi(R_2^2-R_0^2)P_a}{h_0}$	$\frac{\eta(R_2^2-R_0^2)}{h_0^2 P_a}$
1D annular film	$\sigma_s = 1/3, L_2' = 1.25$	$\frac{1.031\eta\pi(R_2^2-R_0^2)(R_2-R_0)^2}{h_0^3}$	$\frac{2.008\pi(R_2^2-R_0^2)P_a}{h_0}$	$\frac{0.513\eta(R_2^2-R_0^2)}{h_0^2 P_a}$
1D annular film	$\sigma_s = 1/5, L_2' = 1.25$	$\frac{1.050\eta\pi(R_2^2-R_0^2)(R_2-R_0)^2}{h_0^3}$	$\frac{3.158\pi(R_2^2-R_0^2)P_a}{h_0}$	$\frac{0.336\eta(R_2^2-R_0^2)}{h_0^2 P_a}$
1D annular film	$\sigma_s = 1/7, L_2' = 1.25$	$\frac{1.058\eta\pi(R_2^2-R_0^2)(R_2-R_0)^2}{h_0^3}$	$\frac{4.324\pi(R_2^2-R_0^2)P_a}{h_0}$	$\frac{0.245\eta(R_2^2-R_0^2)}{h_0^2 P_a}$
1D annular film	$\sigma_s = 1, L_2' = 2.0$	$\frac{\eta\pi(R_2^2-R_0^2)(R_2-R_0)^2}{h_0^3}$	$\frac{\pi(R_2^2-R_0^2)P_a}{h_0}$	$\frac{\eta(R_2^2-R_0^2)}{h_0^2 P_a}$
1D annular film	$\sigma_s = 1/3, L_2' = 2.0$	$\frac{1.041\eta\pi(R_2^2-R_0^2)(R_2-R_0)^2}{h_0^3}$	$\frac{1.901\pi(R_2^2-R_0^2)P_a}{h_0}$	$\frac{0.547\eta(R_2^2-R_0^2)}{h_0^2 P_a}$
1D annular film	$\sigma_s = 1/5, L_2' = 2.0$	$\frac{1.064\eta\pi(R_2^2-R_0^2)(R_2-R_0)^2}{h_0^3}$	$\frac{2.940\pi(R_2^2-R_0^2)P_a}{h_0}$	$\frac{0.362\eta(R_2^2-R_0^2)}{h_0^2 P_a}$
1D annular film	$\sigma_s = 1/7, L_2' = 2.0$	$\frac{1.075\eta\pi(R_2^2-R_0^2)(R_2-R_0)^2}{h_0^3}$	$\frac{4.003\pi(R_2^2-R_0^2)P_a}{h_0}$	$\frac{0.268\eta(R_2^2-R_0^2)}{h_0^2 P_a}$

In order to verify the accuracy of the transfer function, Figures 19 and 20 illustrate the difference in dimensionless stiffness and damping coefficients between the fitted transfer function and numerically calculated Reynolds equation result. The figures show that the fitting results are relatively consistent in the low-frequency region, and the stiffness value obtained in the high frequency region is relatively higher.

The above calculations illustrate the dynamic characteristics of the flat air film in the frequency domain. By transforming them into the time domain, the accuracy of parameter fitting can also be evaluated through a step response. Assume that the boundary structure of an air film is subjected to an impact, and the upper plate produces a displacement $h_1(t) = h_u u(t)$ in an instant, where $u(t)$ represents a unit step function. From the definition of stiffness, the force generated by the air film on the upper plate can be obtained:

$$W_1(t) = \mathcal{L}^{-1}\{-K_b(s)h_1(s)\} = \mathcal{L}^{-1}\{-\frac{As}{\tau s + 1}\frac{h_u}{s}\} = -\frac{Ah_u}{\tau}u(t)e^{-\frac{t}{\tau}} = -K_\infty h_u u(t)e^{-\frac{t}{\tau}} \tag{47}$$

Obviously, the force on the upper plate is an exponential decay function, and its decay constant is the time constant τ.

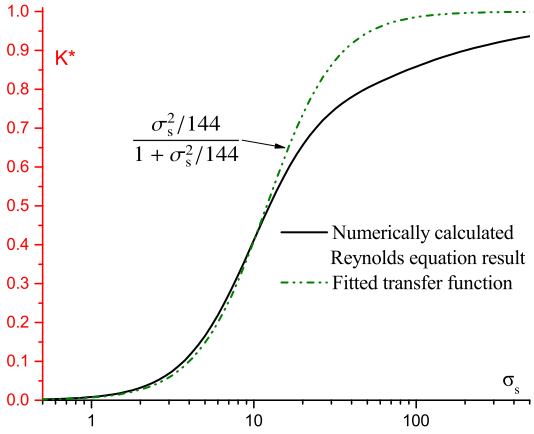

Figure 19. Fitted transfer function of dimensionless stiffness.

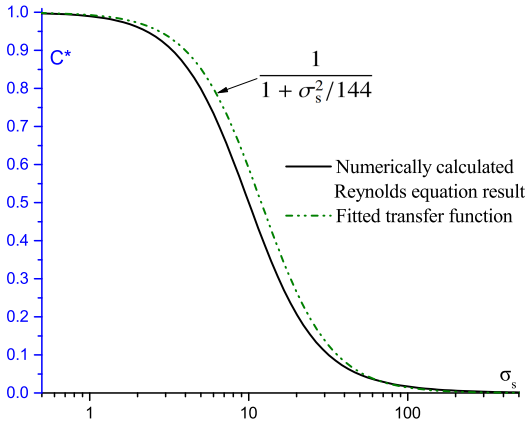

Figure 20. Fitted transfer function of dimensionless damping.

Figure 21 shows the time-domain response calculated by the FEM and the response curve obtained by inversely transforming the fitted function. Note that this figure uses dimensionless units: the ordinate represents the ratio of the air film force to $K_\infty h_u$, and the abscissa represents the ratio of time to the decay constant τ, so the fitting result curve is identical to that in Figure 21a,b. It can be seen that the fitting results can represent the characteristics of thin gas films well. Figure 21b also shows the calculation results of the FEM at different step amplitudes. When the amplitude of the gap variation h_u accounts for a small proportion of gas film gaps (in the figure, this value is 0.1% of h_0), the response amplitude is highly consistent with the result of linear fitting. As the amplitude of the gap variation accounts for a large proportion, a nonlinear effect gradually appears, but the shape of the response curve also approximates an exponential decay form, even when the amplitude increases to 10% of h_0.

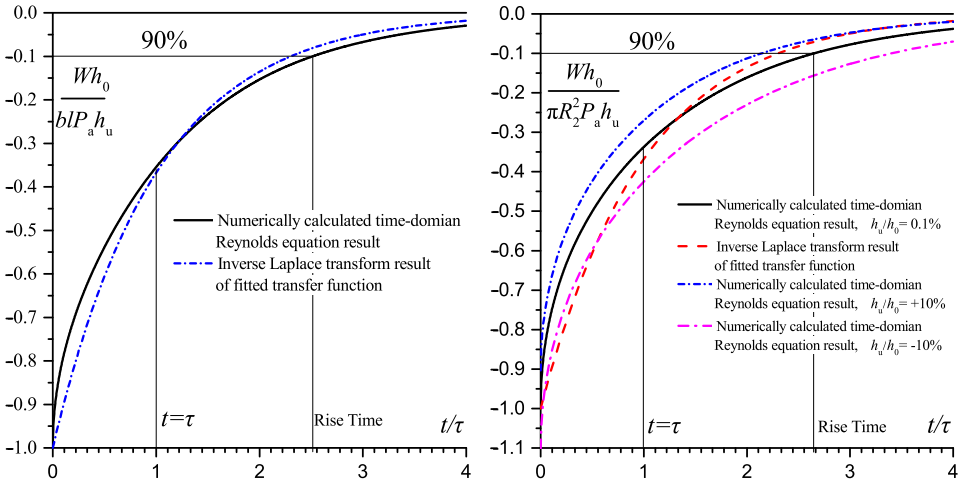

(**a**) 1D flat film (**b**) 1D circular ring

Figure 21. The time-domain response calculated by the FEM and obtained by inversely transforming the fitted function.

6. Conclusions

In contrast to the equations representing the squeeze film effect with the same pressure boundary conditions, a group of dynamic Reynolds equations with stiffness and damping pressure were derived, and parallel flat and circular thin films were analyzed considering a high-pressure boundary. The following conclusions can be drawn:

(1) The various dynamic pressure distribution and stiffness curves of the circular thin film were obtained by calculations of the supply pressure both inside and outside the boundary. The characteristics of the squeeze films with and without external pressure were compared.

(2) The squeeze effect of compressible lubricants causes damping at a zero frequency and stiffness at an infinite-frequency. Due to the influence of gas compressibility, the dynamic pressure is still high at high frequencies. The crossover squeeze number, which indicates the frequency at which the stiffness and the damping force are the same, is equal to 10 given a one-dimensional flat plate and 6 given a parallel disc with an atmospheric boundary. The crossover squeeze number increases when the supplying pressure becomes larger.

(3) Based on our models, the fitting results of the time-domain response calculated by the FEM matches well with the response curve obtained by inversely transforming the fitted function. Both accurately represent the characteristics of a thin gas film. As the amplitude of the gap variation accounts for a large proportion, a nonlinear effect gradually appears, but the shape of the response curve approximates an exponential decay form, even when the amplitude increases to 10% of the gas film thickness.

Author Contributions: Conceptualization, Y.W. and Z.Q.; methodology, Y.W.; software, Y.W.; validation, Y.W., J.X. and W.C.; formal analysis, J.X.; investigation, Y.W.; resources, J.X.; data curation, Z.Q.; writing—original draft preparation, Y.W.; writing—review and editing, J.X.; visualization, W.C.; supervision, Z.Q. and B.W.; project administration, B.W.; funding acquisition, Z.Q. All authors have read and agreed to the published version of the manuscript.

Funding: This work was supported by the Open Project Program of the State Key Laboratory of Applied Optics (SKLAO2021001A05); National Natural Science Foundation of China (No. 51905130); Heilongjiang Provincial Natural Science Foundation of China (No. LH2020E039).

Institutional Review Board Statement: Not applicable.

Informed Consent Statement: Not applicable.

Data Availability Statement: Data available on request from the authors.

Conflicts of Interest: The authors declare no conflict of interest.

Abbreviations

The following abbreviations are used in this manuscript:

η	Viscosity of lubricants (Pa·s)
ω	Exciting frequency (rad/s)
σ	Reciprocal of dimensionless supply air pressure
σ_s	Squeeze number
σ_{sc}	Cut-off frequency
∇	Laplacian operator
Ω	Thin-film domain
h	Film thickness (μm)
j	Unit of imaginary number
l	Length of gas film (m)
t	Time (s)
C	Damping of air bearing (N·s/m)
K	Stiffness of air bearing (N/m)
K_b	Dynamic stiffness (N/m)
K_∞	Ultimate stiffness (N/m)
R_0	Radius of inner annular film (m)
R_2	Radius of outer annular film (m)
L_1'	Ratio of the outer and inner diameters of annular air film
P_a	Ambient pressure (bar)
P_{abs}	Absolute pressure (Pa)
P_d	High pressure (bar)
W	Load-carrying capacity (N)
Subscripts	
0	Steady-state item
1	Dynamic item
s	Real part
c	Imaginary part
Superscript	
$\tilde{}$	Complex variables
$*$	Dimensionless variable

References

1. Wardle, F. *Ultra-Precision Bearings*; Elsevier: Cambridge, UK, 2015; pp. 227–306.
2. Walford, T.; Stone, B. The sources of damping in rolling element bearings under oscillating conditions. *Proc. Inst. Mech. Eng. Part C J. Mech. Eng. Sci.* **1983**, *197*, 225–232. [CrossRef]
3. Wensing, J.A. On the Dynamics of Ball Bearings. Ph.D. Thesis, University of Twente, Enschede, The Netherlands, 1998.
4. Bao, M.; Yang, H. Squeeze film air damping in MEMS. *Sens. Actuators Phys.* **2007**, *136*, 3–27. [CrossRef]
5. Albarbar, A.; Mekid, S.; Starr, A.; Pietruszkiewicz, R. Suitability of MEMS accelerometers for condition monitoring: An experimental study. *Sensors* **2008**, *8*, 784–799. [CrossRef]
6. Wenbin, L.; Jianfeng, H.; Jie, F.; Liyun, C.; Chunyan, Y.; Wenjing, W. Simulation of the engagement of carbon fabric wet clutch: Analytical and experimental comparison. *Tribol. Int.* **2015**, *90*, 502–508. [CrossRef]
7. Jang, S. Manipulating Frictional Performance of Wet Clutch Engagement through Material Properties and Operating Conditions. *Lubricants* **2022**, *10*, 225. [CrossRef]
8. Kane, M.; Do, M.T.; Cerezo, V.; Rado, Z.; Khelifi, C. Contribution to pavement friction modelling: An introduction of the wetting effect. *Int. J. Pavement Eng.* **2019**, *20*, 965–976. [CrossRef]
9. Gronqvist, R. Mechanisms of friction and assessment of slip resistance of new and used footwear soles on contaminated floors. *Ergonomics* **1995**, *38*, 224–241. [CrossRef]
10. Zeidan, F.Y.; Andres, L.S.; Vance, J.M. Design Furthermore, Application of Squeeze Film Dampers in Rotating Machinery. In Proceedings of the 25th Turbomachinery Symposium, Texas A&M University, Turbomachinery Laboratories, College Station, TA, USA, 13 December 1996; pp. 1–20. [CrossRef]
11. Biet, M.; Giraud, F.; Lemaire-Semail, B. Squeeze film effect for the design of an ultrasonic tactile plate. *IEEE Trans. Ultrason. Ferroelectr. Freq. Control* **2007**, *54*, 2678–2688. [CrossRef] [PubMed]

12. Sadd, M.H.; Stiffler, A.K. Squeeze Film Dampers: Amplitude Effects at Low Squeeze Numbers. *J. Eng. Ind.* **1975**, *97*, 1366–1370. [CrossRef]
13. Salbu, E.O.J. Compressible Squeeze Films and Squeeze Bearings. *J. Basic Eng.* **1964**, *86*, 355–364. [CrossRef]
14. Langlois, W. Isothermal squeeze films. *Q. Appl. Math.* **1962**, *20*, 131–150. [CrossRef]
15. Gross, W.A. *Gas Film Lubrication*; John Wi1ey and Sons, Inc.: New York, NY, USA, 1962; pp. 308–317.
16. Pan, C.H.T. The Gaseous Squeeze-Film at Moderately Large Squeeze Numbers. *J. Basic Eng.* **1970**, *92*, 766–781. [CrossRef]
17. Blech, J.J. On isothermal squeeze films. *J. Tribol.* **1983**, *105*, 615. [CrossRef]
18. Talukder, H.; Stowell, T. Pneumatic hammer in an externally pressurized orifice-compensated air journal bearing. *Tribol. Int.* **2003**, *36*, 585–591. [CrossRef]
19. Grossman, R.L. Application of Flow and Stability Theory to the Design of Externally Pressurized Spherical Gas Bearings. *J. Basic Eng.* **1963**, *85*, 495–502. [CrossRef]
20. Holmes, M.H. *Introduction to Perturbation Methods*; Springer Science & Business Media: New York, NY, USA, 2012; Volume 20, pp. 57–73.
21. Licht, L.; Elrod, H. A Study of the Stability of Externally Pressurized Gas Bearings. *J. Appl. Mech.* **1960**, *27*, 250–258. [CrossRef]
22. Boffey, D.A. A Study of the Stability of an Externally-Pressurized Gas-Lubricated Thrust Bearing with a Flexible Damped Support. *J. Lubr. Technol.* **1978**, *100*, 364–368. [CrossRef]
23. Boffey, D.A.; Desai, D.M. An experimental investigation into the rubber-stabilization of an externally-pressurized air-lubricated thrust bearing. *J. Lubr. Technol.* **1980**, *102*, 65–70. [CrossRef]
24. Stiffler, A.K. Analysis of the Stiffness and Damping of an Inherently Compensated, Multiple-Inlet, Circular Thrust Bearing. *J. Lubr. Technol.* **1974**, *96*, 329–336. [CrossRef]
25. Stiffler, A.K.; Smith, D.M. Dynamic Characteristics of an Inherently Compensated, Square, Gas Film Bearing. *J. Lubr. Technol.* **1975**, *97*, 52–62. [CrossRef]
26. Miyatake, M.; Yoshimoto, S. Numerical investigation of static and dynamic characteristics of aerostatic thrust bearings with small feed holes. *Tribol. Int.* **2010**, *43*, 1353–1359. [CrossRef]
27. Bhat, N.; Kumar, S.; Tan, W.; Narasimhan, R.; Low, T.C. Performance of inherently compensated flat pad aerostatic bearings subject to dynamic perturbation forces. *Precis. Eng.* **2012**, *36*, 399–407. [CrossRef]
28. Colombo, F.; Raparelli, T.; Trivella, A.; Viktorov, V. Identification of a Lumped Parameters Numerical Model of Gas Bearings: Analysis of 1D Parallel Plates. In Proceedings of the Advances in Italian Mechanism Science, Cassino, Italy, 10 December 2019; pp. 467–473. [CrossRef]
29. Belforte, G.; Colombo, F.; Raparelli, T.; Trivella, A.; Viktorov, V. Study of the Static and Dynamic Performance of Rectangular Air Pads by Means of Lumped Parameters Models. In Proceedings of the ASME 2012 11th Biennial Conference on Engineering Systems Design and Analysis, Nantes, France, 2–4 July 2012.
30. Colombo, F.; Lentini, L.; Raparelli, T.; Trivella, A.; Viktorov, V. Dynamic characterisation of rectangular aerostatic pads with multiple inherent orifices. *Tribol. Lett.* **2018**, *66*, 1–13. [CrossRef]
31. Moradi, M.; Colombo, F.; Raparelli, T.; Trivella, A.; Viktorov, V. Dynamic lumped model of externally pressurized rectangular air bearings. *Precis. Eng.* **2019**, *56*, 101–112. [CrossRef]
32. Hamrock, B.J.; Schmid, S.R.; Jacobson, B.O. *Fundamentals of Fluid Film Lubrication*; Marcel Dekker, Inc.: New York, NY, USA, 2004; pp. 202–228.
33. Wu, Y.; Qiao, Z.; Xue, J.; Liu, Y.; Wang, B. Root iterative method for static performance analysis of aerostatic thrust bearings with multiple pocketed orifice-type restrictors based on ANSYS. *Ind. Lubr. Tribol.* **2019**, *72*, 165–171. [CrossRef]
34. Castelli, V.; Pirvics, J. Review of numerical methods in gas-bearing film analysis. *Tribology* **1969**, *2*, 76. [CrossRef]
35. Shi, J.; Cao, H.; Jin, X. Investigation on the static and dynamic characteristics of 3-DOF aerostatic thrust bearings with orifice restrictor. *Tribol. Int.* **2019**, *138*, 435–449. [CrossRef]
36. Bathe, K.J. *Finite Element Procedures*; Prentice-Hall, Inc.: Hoboken, NJ, USA, 1996; pp. 642–694.
37. Wu, Y.; Qiao, Z.; Xue, J.; Wang, B.; Chen, W. A newly treated boundary conditions to enhance accuracy of finite element analysis for orifice-type aerostatic bearings. *Adv. Eng. Softw.* **2022**, *173*, 103277. [CrossRef]